ACS chemical biology

Articles

Cite This: ACS Chem. Biol. 2019, 14, 2585−2594

pubs.acs.org/acschemicalbiology

Surprising Non-Additivity of Methyl Groups in Drug−Kinase Interaction

Barbara Wienen-Schmidt,[‡] Denis Schmidt,[†] Hans-Dieter Gerber,[‡] Andreas Heine,[‡] Holger Gohlke,[†,§] and Gerhard Klebe*[,‡]

[‡]Institut für Pharmazeutische Chemie, Philipps-Universität Marburg, Marbacher Weg 6, 35032 Marburg, Germany

[†]Mathematisch-Naturwissenschaftliche Fakultät, Institut für Pharmazeutische und Medizinische Chemie, Heinrich-Heine-Universität Düsseldorf, 40225 Düsseldorf, Germany

[§]John von Neumann Institute for Computing (NIC), Jülich Supercomputing Centre (JSC) and Institute for Complex Systems - Structural Biochemistry (ICS 6), Forschungszentrum Jülich GmbH, Jülich, Germany

Supporting Information

ABSTRACT: Drug optimization is guided by biophysical methods with increasing popularity. In the context of lead structure modifications, the introduction of methyl groups is a simple but potentially powerful approach. Hence, it is crucial to systematically investigate the influence of ligand methylation on biophysical characteristics such as thermodynamics. Here, we investigate the influence of ligand methylation in different positions and combinations on the drug−kinase interaction. Binding modes and complex structures were analyzed using protein crystallography. Thermodynamic signatures were measured via isothermal titration calorimetry (ITC). An extensive computational analysis supported the understanding of the underlying mechanisms. We found that not only position but also stereochemistry of the methyl group has an influence on binding potency as well as the thermodynamic signature of ligand binding to the protein. Strikingly, the combination of single methyl groups does not lead to additive effects. In our case, the merger of two methyl groups in one ligand leads to an entirely new alternative ligand binding mode in the protein ligand complex. Moreover, the combination of the two methyl groups also resulted in a nonadditive thermodynamic profile of ligand binding. Molecular dynamics (MD) simulations revealed distinguished characteristic motions of the ligands in solution explaining the pronounced thermodynamic changes. The unexpected drastic change in protein ligand interaction highlights the importance of crystallographic control even for minor modifications such as the introduction of a methyl group. For an in-depth understanding of ligand binding behavior, MD simulations have shown to be a powerful tool.

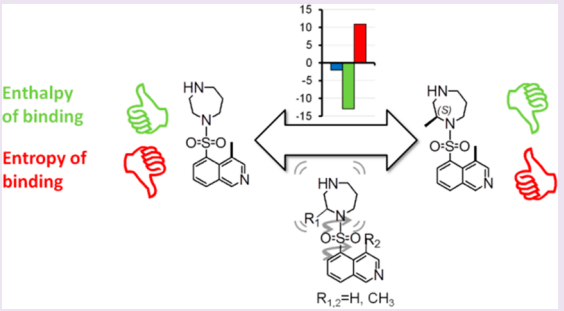

In the process of drug design and drug optimization, lead structures can be decorated with a broad range of functional groups and chemical building blocks in order to improve binding potency and biophysical characteristics. As a matter of fact, design that simultaneously considers well-tailored biophysical properties has become increasingly popular over the past years.[1−6] This development is based on the assumption that additional binding characteristics such as binding thermodynamics and kinetics may help to accelerate and improve the development and prediction of clinically successful drugs. Thereby, the introduction of a methyl group to a ligand is a simple but potentially highly effective approach. The importance but also the enormous popularity of methyl groups in drug design has been reported and reviewed previously.[7,8] The replacement of a hydrogen by a methyl group can significantly alter structure−activity relationships. These changes have the goal to improve electrostatics, modulated polarity, and steric complementarity as well as to tailor conformational energetics and restrict the ligand's geometry in the bound state. Moreover, ordered water molecules in the protein active site that are replaced or shifted as a consequence of the presence of a methyl group can take a major impact on structure−activity relationships.[7] In rare cases, the introduction of an additional methyl group can even boost activity of a ligand 500 fold.[7,9] On the other hand, it can also reduce activity drastically if added at the wrong position.[7]

Here, we present a study where the influence of methyl groups on drug−kinase interactions is thoroughly investigated. Therefore, cAMP-dependent protein kinase (PKA) is used as a model protein, allowing the use of a wide range of experimental techniques. The ligands presented in this study comprise two prominent kinase inhibitors: Fasudil and H-1152.[10−17] In addition, we studied "chimeric" ligands showing methyl groups at different positions of the parent scaffold. An overview of the chemical structures of all five ligands is given in

Received: June 17, 2019
Accepted: October 22, 2019
Published: October 22, 2019

DOI: 10.1021/acschembio.9b00476
ACS Chem. Biol. 2019, 14, 2585−2594

Figure 1. H-1152 (**1**) represents a dimethylated analogue of fasudil (**5**), the latter being the nonmethylated reference ligand

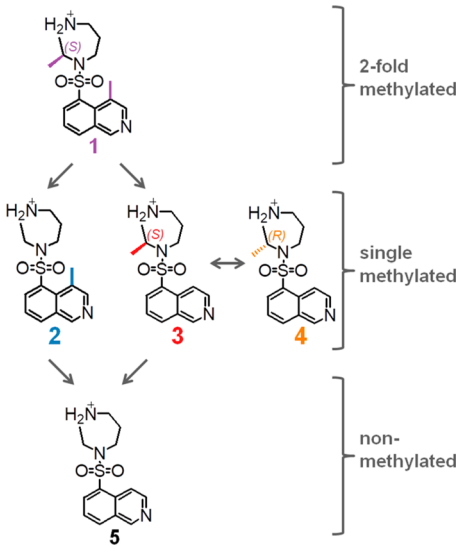

Figure 1. Overview of all ligands discussed. Different methylation positions were investigated. Ligand H-1152 (**1**) displays two methylated sites, one at the isoquinoline moiety and a second at the homopiperazine portion. These two sites were separately investigated via analysis of **2** and **3**. In order to examine the influence of the spatial position of the methyl group of **3**, its stereoisomer **4** was additionally studied. Fasudil (**5**) was used as the nonmethylated reference.

presented previously.[18] The two different singly methylated ligands that derive from H-1152 are **2** and **3**. Ligand **2** is methylated at the 4-position of the isoquinoline portion, and **3** is methylated at the 2-position of the homopiperazine ring. The latter methyl group in **3** introduces a stereogenic center which exhibits for both **1** and **3** an *S* configuration. In order to evaluate the influence of this methyl group in an inverted configuration, **4** with an *R* configuration was added to the panel.

Crystal structures of all ligands depict differences in binding modes and suggest nonadditivity with respect to the geometric influence of the added methyl groups. Nonadditivity is also observed for the binding thermodynamics. Thermodynamic data were measured using isothermal titration calorimetry (ITC). Not only is the binding potency ΔG influenced by the different methylation patterns but also the partitioning in enthalpic and entropic contribution is modulated. The crystal structure of the dimethylated H-1152 reveals an alternative binding mode compared to fasudil. Multiple crystal structures of bovine PKA, bovine PKA mutants, and rho-kinase 1 in complex with H-1152 have been published; however, none of them reports this alternative binding orientation as described in this report.[14,19,20] Most interestingly, this binding mode is similar to that found with the kinase Roco4 in complex with H-1152. Roco4 is a model protein for the human leucine-rich-repeat kinase 2 (LRRK2) which has been described to be involved in late-onset Parkinson's.[21]

Strikingly, this alternative binding orientation is not observed for any other ligand of this series in complex with PKA. This drastic change in protein−ligand interaction is likely to cause a strong difference in ligand binding properties toward PKA.

To better understand the conformational properties of the studied ligands in solution and the impact that the methyl groups attached at different sites have on the structural dynamics, we performed molecular dynamics (MD) simulations expanding over several microseconds. We used three characteristic motions to describe the ligands' conformational spaces: (i) rotations about the two adjacent dihedral angles connecting both ring systems via the central sulfur atom, thus determining the relative orientation of the two ring moieties, (ii) the puckering of the seven-membered homopiperazine ring, and (iii) a bending motion of the isoquinolinyl moiety that manifests the out-of-plane movement of the attached substituents, R_1, and the central sulfur atom. We characterized the three motions by computing the conformational Gibbs free energies of the conformers found in the crystal and in the free solution forms. Furthermore, we estimated the conformational entropy resulting from the three motions to investigate by how much the methylation pattern restricts the accessible conformational space in solution.

RESULTS AND DISCUSSION

Crystal Structures Reveal Surprising Binding Mode.

Co-crystal structures with resolutions between 1.4 and 1.5 Å could be obtained. The crystal structure of **5** has already been published by us in a previous contribution.[18] All structures were deposited in the Protein Data Bank (PDB). The respective PDB codes are listed in Table 1.

Table 1. Protein Data Bank (PDB) Codes of All Five Co-Crystal Structures

ligand	PDB code
1	5M6V
2	5M6Y
3	5M75
4	5M71
5	5LCP

An overview and superposition of the different ligands is depicted in Figure 2. The hinge binding modes of ligands **2**, **3**, **4**, and **5** are all, as expected, similar (Figure 2A). Surprisingly, ligand **1** deviates from this pattern and populates two distinct binding poses (Figure 2B). Apart from the first orientation, which agrees with the hinge binding mode observed for the other ligands, **1** exhibits a second, alternative interaction pattern with the hinge, where the ligand is flipped over and rotated, with respect to the first, by about 60°. Figure 3 displays a schematic overview of the hinge binding portion of the different ligands for ease of visualization. Interestingly, the alternative binding orientation of **1** is the only case where a hydrogen bond between one of the sulfonyl oxygens and Thr183 of the protein is formed.

A superposition of all five ligands (Figure 2C) shows that also the homopiperazine moiety of the ligand adopts different ring conformations depending on the methylation (see Results on homopiperazine puckering for a detailed discussion). This, in turn, has severe consequences on the hydrogen-bonding pattern formed by the respective ligands (Figure 4). While the homopiperazine portions of **1** (Figure 4A), **2** (Figure 4B), and **5** (Figure 4E) form several direct hydrogen bonds to the protein, none are formed by **3** (Figure 4C) and **4** (Figure 4D). However, all ligands form in all adopted poses a hydrogen bond between their respective isoquinoline nitrogen and the

DOI: 10.1021/acschembio.9b00476
ACS Chem. Biol. 2019, 14, 2585−2594

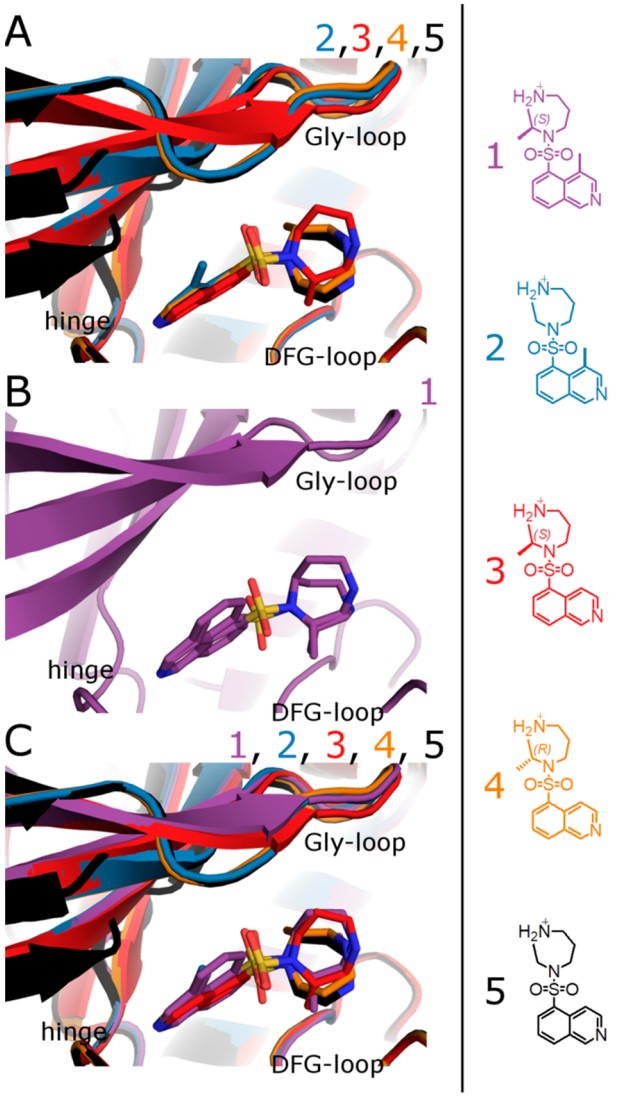

Figure 2. Cocrystal structures of the different ligands. (A) Superposition of complex structures of ligands **2**, **3**, **4**, and **5**. All ligands share a common hinge binding mode. (B) Complex structure of **1**. Ligand **1** binds in two different conformations. (C) Superposition of all ligands **1**–**5** (colors according to the color codes used for the formulas on the right, heteroatoms type-coded, N blue, O red, S yellow).

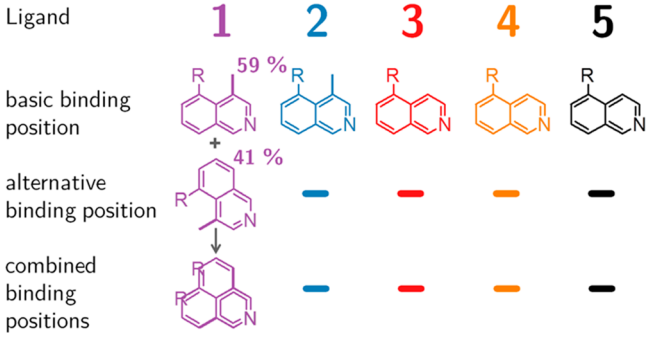

Figure 3. Schematic hinge binding pattern. All five ligands show a common basic hinge binding pose. However, ligand **1** shows an additional alternative pose where the ligand is flipped over and rotated by about 60° which is 41% populated. Color coding corresponds to the ligand numbering scheme.

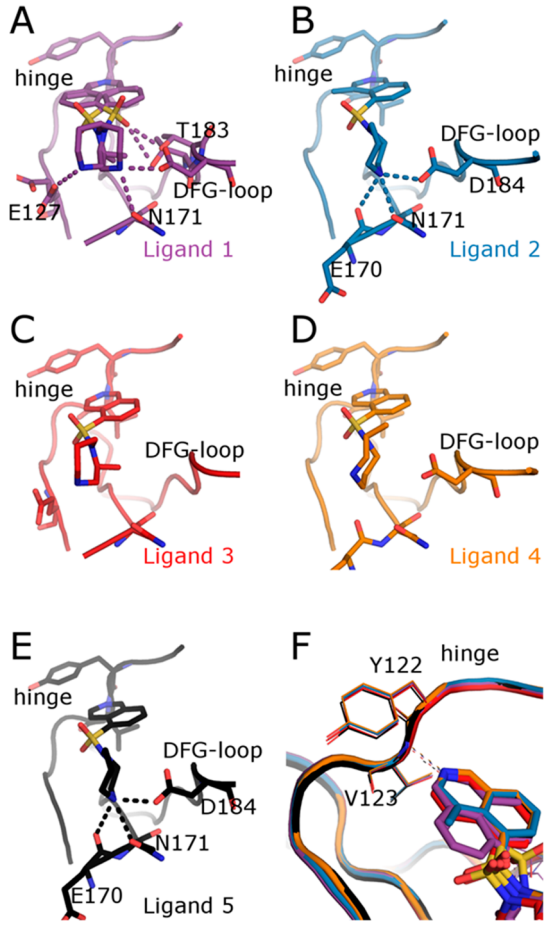

Figure 4. Protein–ligand hydrogen bonding patterns. Dotted lines indicate hydrogen bonds. (A) 2-fold methylated ligand **1** in complex with PKA, both conformers form three different hydrogen bonds with the protein. Respective occupancies are 51% of conformation A and 49% of conformation B. (B) Ligand **2** in complex with PKA. A total of four hydrogen bonds are formed. (C) Complex structure of *S*-configurated **3**, only one hydrogen bond is formed to the hinge (see F). (D) *R*-configured **4** complexed with PKA, also here one hydrogen bond is formed to the hinge (see F). (E) Unmethylated **5** forms four hydrogen bonds to PKA. (F) Superposition of the hinge-binding motif of all ligands.

backbone nitrogen of Val123, which is part of the hinge region of the protein (Figure 4F). Interestingly, one of the configurations of homopiperazinyl of **1** resembles the one of **3**, which is in line with the identical stereochemistry of the attached methyl group. However, the hydrogen bond of **1**, the homopiperazinyl nitrogen to the carboxylate group of Glu127, does not occur in the complex with **3**. This is due to the absence of the second alternative side-chain conformation of Glu127 in the complex of **3** (Figure 4A,C). It must be noted that homopiperazinyl positions 3 and 7 of the two bound conformations of **1** coincide (Figure S13). As a consequence, positions 4, 5, and 6 of the homopiperazinyl ring cannot be unequivocally assigned to the different configurations. Thus, two potential pairs of configurations exist, A/B and A′/B′, which only differ in these three positions (Figure S13). Configurations A/B have been chosen due to the better observed densities after refinement.

For **4**, the inverted enantiomer of **3**, the homopiperazine ring adopts a flipped conformation, which is highly similar with respect to the occupied space compared to fasudil (**5**), but the

DOI: 10.1021/acschembio.9b00476
ACS Chem. Biol. 2019, 14, 2585–2594

nitrogen is located in a different position. This altered nitrogen position of **4** leads to the disruption of the hydrogen bonds observed in the complex structure of **1**. This leaves both the complexes of ligands **3** and **4** with a total of a single hydrogen bond to the protein (Figure 4F).

Nonadditivity of the Thermodynamic Signatures. ITC data were used to analyze the binding thermodynamics of the different ligands to the protein. Figure 5 gives an overview of the measured thermodynamic signatures. The profile of the doubly methylated ligand **1** (H-1152) is not an additive combination of the profiles of the two singly methylated ligands **2** and **3**. This is in accordance with the crystallographic data that demonstrate a distribution of **1** over two alternative binding modes, whereas **2** and **3** each adopt only one orientation. This disorder provides ligand **1** with an entropic advantage over the other two ligands, although other effects concerning the unbound ligand or desolvation differences may contribute to the entropy differences.

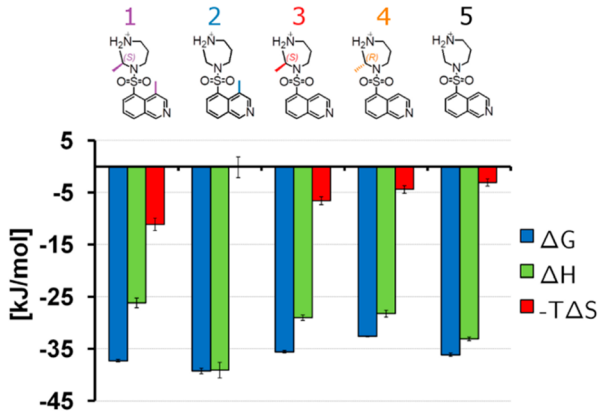

Figure 5. Thermodynamic signatures for ligands **1**−**5**. Binding potency represented by Gibbs free energy (ΔG) and the partitioning in enthalpy (ΔH) and entropy ($-T\Delta S$) changes as a consequence of the attached methyl groups. Ligand **2** is the most potent and enthalpically favored binder. The data of **5** have been added from a previous study by us.[18]

Methylation at Isoquinoline Portion Is Most Favorable. When thermodynamic binding profiles of the three differently singly methylated ligands are compared to that of the nonmethylated fasudil (**5**), modulations in affinity as well as in enthalpy and entropy are observed. Methylation solely at the homopiperazine reduces enthalpic contributions and overall affinity, while the entropic contributions slightly increase. Methylation solely at the isoquinoline moiety, on the other hand, leads to an improved affinity for enthalpy reasons. The methyl group is placed in a highly hydrophobic environment of the protein-binding site (Leu49, Phe327). This enables the formation of additional van-der-Waals contacts between ligand and PKA without displacing a water molecule. Hence, this factor will promote enthalpy-driven binding.[22]

Next to the static observations in the crystal structures, conformational dynamics of the ligands might influence the thermodynamic profiles in addition to differences which might arise for the desolvation of the individual ligands in solution and the resolvation of the ligands in their protein-bound states. These contributions need to be regarded if a quantitative comparison with the experimental binding affinity is intended. As the impact of methylation at the parent ligand scaffold was put into focus in this contribution, we decided to investigate for a qualitative comparison the conformational properties in more detail. Therefore, to determine the conformational free energy differences between the unbound and bound conformations and the influence of the methylation patterns on the conformational entropies, MD simulations of the ligands in solution were performed.

Conformational Space of Unmethylated Fasudil Reference. The overall conformation of the ligands under investigation can be expressed by the dihedral angles θ_1 and θ_2. These angles describe the orientation of the homopiperazinyl and the isoquinolinyl ring relative to each other (Figure 6B). Together, these angles allow the comparison of the observed conformations in the crystal structures with the overall accessible conformational space in solution. Figure 6A shows the two-dimensional free energy landscapes for the θ_1/θ_2 angles, which were derived from the simulations of the respective ligands.

For the unmethylated ligand **5**, the θ_1/θ_2 space shows an inversion symmetry around the origin with four local minima (denoted I, II, I*, and II*, where I* and II* are mirror images of I and II, respectively, Figure 6A, top left panel). This inversion symmetry reflects the achirality of **5** and demonstrates that our conformational sampling was sufficiently exhaustive in regions up to ∼30 kJ mol^{-1} above the global minimum. States I/II are located at $\theta_1 = -60°/60°$, such that the ligand is in a "compact" conformation (Figure 6C). In this conformation, one of the two sulfonamide oxygens is in-plane with the isoquinolinyl moiety (Figure 6C). For θ_2, values of $50°/-170°$ are preferred, but a rotation around the respective bond is possible, which corresponds to an interconversion between I and II as well as I* and II*, respectively (gray arrows in Figure 6A, top left panel). The transition between the symmetry-related groups (i.e., I/II to I*/II*) requires a concerted motion, consisting of a θ_1 rotation that brings the molecule into an "extended" transition conformation. In this extended conformation, the homopiperazinyl moiety points away from the isoquinolinyl moiety ($\theta_1 = 180° \pm 60°$). Simultaneously, θ_2 passes ±90° (gray arrows in Figure 6A, top left panel). The PKA-bound conformation of **5** does not correspond to a local minimum in the θ_1−θ_2 space but is located along one of these transition paths. It is energetically disfavored with respect to the global minimum (Figure 6A, Figure 7A).

Influence of Methylation on Overall Conformational Dynamics. The simulations of **3** and **4** reveal a similar shape of the conformational space with respect to θ_1 and θ_2 and identical localization of the minima as compared to **5** (Figure 6A, top middle and right panel). However, the chirality of **3** and **4** due to methylation at the homopiperazine scaffold (R_2 = Me) causes a loss of inversion symmetry, particularly visible for states I and I*. As a consequence, the θ_1/θ_2 maps of both enantiomers are mirror symmetrical, again demonstrating converged conformational sampling in regions up to ∼30 kJ mol^{-1} above the global minimum. Compared to the achiral **5**, the methylation hampers the θ_2 rotation by increasing the energy barrier at $\theta_1 = \theta_2 = \pm 90°$ (red dashed lines in Figure 6A, top middle and right panel). Similarly, the transitions along $\theta_1/\theta_2 = -150/70°$ and $\theta_1/\theta_2 = 150/-70°$ for **3** and **4**, respectively, are disfavored (red arrows in Figure 6A, top panel). This might contribute to the fact that **4** binds to PKA with a flipped homopiperazinyl motif ($\theta_2 = 70°$).

Methylation at the isoquinoline scaffold (**1**, **2**: R_1 = Me) leads to a more pronounced change in the conformational

DOI: 10.1021/acschembio.9b00476
ACS Chem. Biol. 2019, 14, 2585−2594

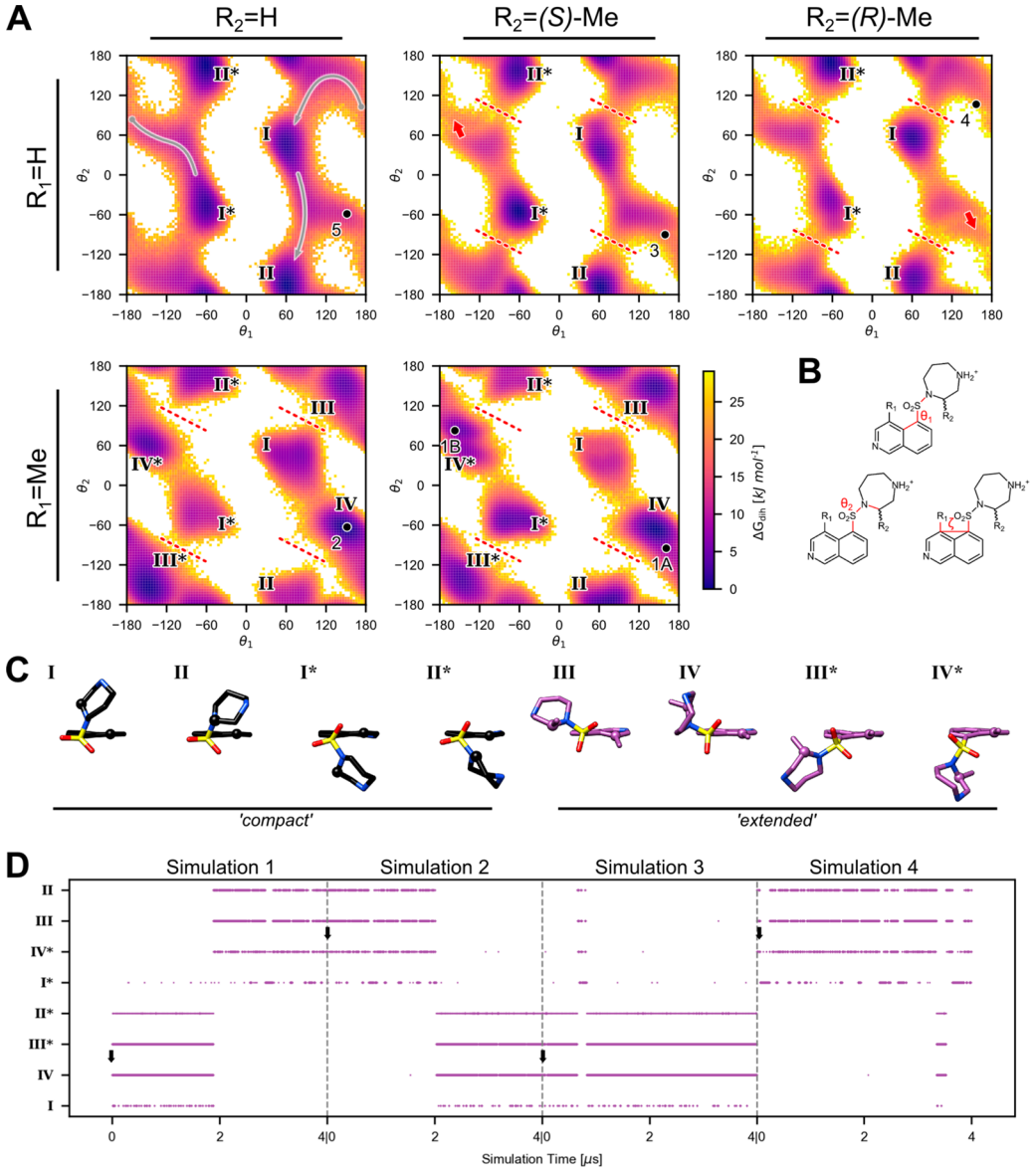

Figure 6. Conformational behavior described by dihedral angles θ_1 and θ_2. (A) Two-dimensional free energy landscape obtained by mapping conformations to the θ_1/θ_2 plane and applying eq 1. Panels are arranged such that compounds with R_1 = H (**5**, **3**, **4**) and R_1 = Me (**2**, **1**) are shown in the top and bottom row, respectively, and compounds with R_2 = H/*S*-Me/*R*-Me (**5**, **2**/**3**, **1**/**4**) are located in the left/middle/right column, respectively. Distinct states are enumerated from I to IV and their symmetry-related states from I* to IV*, respectively. The location(s) of the crystal structures in the dihedral space are indicated by circles and annotated with the compound number. For **1**, both crystal structure conformations are indicated and annotated accordingly. Gray arrows in the top-left panel indicate exemplary pathways that allow interconversion (I to II) and transition between symmetry related conformations (I* to I). Red dashed lines and arrows indicate restrictions in conformational space upon methylation that hamper interconversions and transitions. (B) General structure of fasudil and derivatives, where bonds defining the θ_1, θ_2, and ζ torsions are highlighted in red. (C) Representative conformations of the eight states (I–IV, I*–IV*) observed in the θ_1/θ_2 space. Conformations were selected from the simulations of **5** (black) for states I–II and I*–II* and of **1** (purple) for states III–IV and III*–IV*. Ligands are shown in stick representation such that the isoquinolinyl moiety is arranged horizontally with the line of sight along the isoquinolinyl–sulfur bond. The carbon atoms carrying the variable substituents R_1 and R_2 (C4 of the isoquinolinyl and C2 of the homopiperazinyl) are highlighted by sphere representation. (D) Dihedral state of compound **1** over the course of the combined simulation time. The four simulations are separated along the *x*-axis by gray, vertical, dashed lines. Simulations **1** and **3** (starting at 0 μs and 8 μs, respectively) were started from ligand conformation A in the crystal structure (corresponding to state IV), while simulations **2** and **4** were started from the B conformation (state IV*). The respective starting geometries are indicated by black arrows.

landscape. Two new local minima emerge (III and IV), along with their symmetry-related ones (III* and IV*, Figure 6A, bottom row). Like the methylation at R_2, the methylation at R_1 hampers the θ_2 rotation, but to a larger extent (red dashed lines in Figure 6A, bottom row). In **1**, both methylations contribute to this effect. As a result, two families of conformers emerge, which are either I, IV, III*, and II* or I*, IV*, III, and II. These families of conformers are separated by high energy barriers. As a consequence, the interconversion between these families is rarely observed, even during MD simulations extending over microseconds (Figure 6D), which might explain the existence of two conformers (one per family of conformations) found for **1** in the crystal structure. The newly emerging minima correspond to conformations, where the

DOI: 10.1021/acschembio.9b00476
ACS Chem. Biol. 2019, 14, 2585–2594

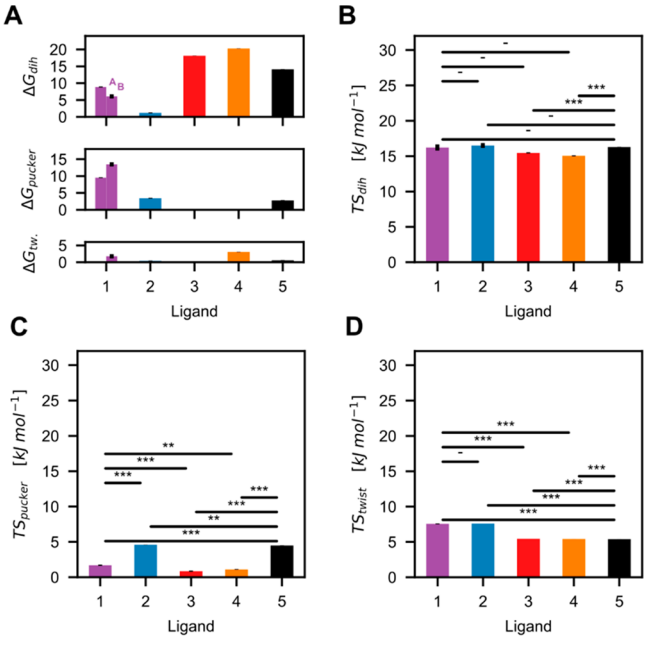

Figure 7. Computed conformational free energies and conformational entropies. (A) Bar plots of conformational free energies of the crystal structures of the five ligands for dihedral state (ΔG_{dih}), puckering state (ΔG_{pucker}), and the twisting motion (ΔG_{tw}). Error bars indicate standard error of the mean over four independent simulations in kJ mol^{-1}. For **1**, the two conformations in the crystal structure are plotted separately and indicated by A and B, respectively. (B–D) Computed conformational entropies over dihedral states (B), puckering states (C), and twisting states (D) for the five ligands. Error bars as in panel A. Significance levels: ***$p \leq 0.001$, **$p \leq 0.01$, *$p \leq 0.05$, (−) $p > 0.05$.

ligands adopt "extended" geometries ($\theta_1 = 180° \pm 60°$, Figure 6C) and the methyl group occupies the space between the sulfonamide oxygen atoms to minimize steric crowding. This steric demand further induces out-of-plane bending motions of the isoquinoline system (Figure S6), which increases the calculated entropy in solution (Figure 7D). The extended conformations resemble the geometries found for the different ligands in the bound state and suggest that the conformers of **1** and **2** in the crystal are energetically favored, as indicated by the lower ΔG_{dih} values compared to those of ligands **3**, **4**, and **5** (Figure 7A).

Together, the methylation of the isoquinoline preorients the ring systems in solution, which yields an extended ligand conformation. This extended conformation is structurally close to the bound and crystallized states, which indicates that this methylation fosters binding. Counterintuitively, while this methylation changes the conformational space, it does not reduce the size of the accessible conformational space judged from the conformational entropy of dihedral rotation TS_{dih} (Figure 7B). Instead, a steric conflict with the sulfonamide oxygen atoms is induced, and the enforced bending of the aromatic moiety increases conformational entropy (Figure 7D, TS_{twist}, **2** versus **5**). Consequently, **2** has the largest conformational entropies of θ_1/θ_2 rotation and twisting (as well as puckering, see next section) in a solution of all five ligands. Thus, it supposedly experiences the largest loss in entropy upon binding. This is consistent with the ITC data, where **2** has the lowest entropic contribution to binding of all five ligands.

Influence of Methylation on Homopiperazinyl Puckering. Next, the puckering states of the homopiperazinyl ring were evaluated. The considered states that can exist in seven-membered rings are chair (C), twisted-chair (TC), boat (B), and twisted-boat (TB), each comprising 14 possible substates.[10] In the free ligand simulations, TC is the most abundant form, populated at 75% of the simulation time, followed by C (about 25%), whereas TB and B are rarely found (each about 0.5%; Supporting Information Figure S7).

The ligands with the unmethylated, i.e., unrestrained, homopiperazinyl moiety (**2** and **5**) bind to PKA with the puckering state TC10, which is supposedly the energetically best state in complex with PKA and allows hydrogen-bond formation with Asp184 as discussed above (Figure 4). In contrast, **3** and **4** bind to PKA with the symmetry-related puckering states TC5 and TC12, respectively, which disallows the formation of these hydrogen bonds. The simulations of unbound **3** and **4** show that the puckering space in solution is strongly dominated by these two states TC5 and TC12 (Supplementary Figure S8). This indicates that the methylation at R_2 causes a strong restriction of the puckering space. In turn, conformational entropy of puckering (TS_{pucker}, but also TS_{dih}) and hence the entropy loss upon binding is reduced. Thus, **3** and **4** are entropically favorable upon binding compared to ligands **2** and **5**, which is again consistent with the ITC data. Furthermore, the differences in puckering free energy between bound and unbound states (Figure 7A, ΔG_{pucker}) are small and promote binding which is counteracted by less favorable interactions with PKA in the bound state. Interestingly, TC5 and TC12 are also the favored puckering states for **2** and **5** in solution, but TC10 (found in the bound state) is disfavored (Supporting Information Table S4). Yet, this energetic penalty is close to thermal energy at $T = 300$ K and may be compensated by interactions with Asp184.

For **1**, as for **3**, the most abundant puckering state in solution is TC5 (consistent with the *S*-configuration of the methyl group in both ligands), while the bound conformations of **1** adopt the puckering states TC4 (**A**) and TC11 (**B**). However, as discussed above, the assignment of the observed electron densities to discrete configurations is difficult. The hypothesized configuration A′ would correspond to the regular hinge binding mode in combination with the most favorable puckering state TC5 (identical binding pose as **3**). As in **3**, this configuration cannot form a salt bridge with Asp184 (but with Glu127). Configuration B′ on the other hand would correspond to the alternative hinge binding mode in combination with the energetically disfavored puckering state TC12 (Supporting Information Table S4) and could form the compensatory salt bridge with Asp184. However, due to the variability of the observed conformations in the crystal structure, a reliable decomposition into the different contributions is not possible.

In all cases, the homopiperazinyl methylation disfavors the extended conformations of the bound state, resulting in a less favorable ΔG_{dih} (Figure 7A, **3** and **4** versus **5** and **1** versus **2**), which could be the cause for the reduced enthalpic contribution to binding as observed in the ITC data.

Overall, **2** is the most potent inhibitor of this series. This ligand profits from a beneficially positioned methyl group in the small hydrophobic niche, which simultaneously locks the ligand in an energetically favorable conformation in solution. Furthermore, it can maintain favorable H-bonds with Asp184. On the other hand, its methylation does not reduce the

DOI: 10.1021/acschembio.9b00476
ACS Chem. Biol. 2019, 14, 2585–2594

conformational space in solution, making the binding of **2** the least entropically favored one.

On the contrary, the methyl groups introduced at the homopiperazinyl portion of **3** and **4** reduce binding potency. While the conformational entropy in solution is reduced, which makes binding entropically more favorable, the homopiperazinyl ring has to adopt in both cases an orientation that ruptures favorable H bonds to be formed to Asp184 and Asn171, which is detrimental to the enthalpic contribution to binding. Additionally, both show an unfavorable conformational free energy. Remarkably, fasudil (**5**), which does establish these H bonds, experiences an enthalpic advantage compared to **3** and **4**, which can presumably be attributed to more favorable conformational free energy. **1** exhibits the profile with the enthalpically least favorable binding and highest entropic benefit. The methylation at R_2 partly counteracts the enthalpically beneficial effect of the methylation at R_1, by slightly forcing the bound geometry away from the conformational optimum. Additionally, it causes a partial loss of interactions of the homopiperazinyl moiety in the bound state, depending on the configuration, as seen for **3** and **4**. However, the disorder over two binding modes provides this ligand with an entropic advantage.

CONCLUSION

Our study shows that not only the region but also the stereospecific attachment of methyl groups matters for binding potency and the thermodynamic inventory. Combination of different ligand methylation sites does not necessarily lead to an additive effect on binding properties observed for the single methylation sites. Although the ligands in question are rather small, the influence of the methylation patterns is surprisingly complex. As observed in our case, a combination can alter the ligand binding mode in a hardly predictable way. Specifically, the data reveal the importance of regio- and stereospecificity as well as the combination of both by methylating one ligand. However, the results underline that it is crucial to factorize in such potentially large effects of small modifications during ligand optimization. Hence, continuous control of binding modes by crystallography is highly advised in the interpretation of experimental data in drug design, even for such small ligand alterations as methylations. Furthermore, MD simulations are a means to unravel the influence of ligand conformational dynamics in the unbound state on the binding potency. In that respect, we identified the preorganization of the ring systems with respect to each other as well as the puckering of the saturated ring as most relevant motions that are modulated by methylation. A surprising observation is the fact that ligand **1** populates in solution two families of conformers, separated by a high energy barrier with rare interconversion rate. This might explain why for this ligand two different conformers, each being representative for one of the families, are found bound in the complex structure with the kinase. Possibly this mirrors an interesting finding often seen in crystallographic studies but rarely accountable by specific properties of the ligands.

Furthermore, the comprehensive and integrative analysis of MD simulations with biophysical data and crystallography allows the investigation of protein−ligand binding from a different perspective, yielding a more complete picture than any of the methods could yield on its own.

METHODS

Protein Expression and Purification. The method of protein expression and purification was previously described.[18,23]

Crystallization. Co-crystallization of **5** has been presented previously.[18] Co-crystallization was performed using the hanging drop method at 4 °C. The crystallization drops contained the following ingredients: 10 mg mL^{-1} PKA (240 μM), 30 mM MBT (MES/Bis-Tris Puffer pH 6.9), 1 mM DTT, 0.1 mM EDTA, 75 mM LiCl, 0.03 mM Mega 8, 0.07 mM PKI (Sigma: P7739), 1.2 mM ligand dissolved in DMSO from a 50−100 mM stock. The well contained a mixture of methanol in water with varying methanol concentrations (v/v) for the different ligands (**1**, 18% methanol; **2**, 20% methanol; **3**, 16% methanol; **4**, 19% methanol). In the crystallization setup, streak-seeding was performed with apo crystals with the help of a horse hair in order to initialize crystal growth. For crystal mounting, crystals were cryo-protected in 5 mM MBT (MES/Bis-Tris buffer pH 6.9), 1 mM DTT, 0.1 mM LiCl, 1.2 mM ligand dissolved in DMSO from a 50−100 mM stock, 16% (v/v) methanol, 30% (v/v) MPD, and flash frozen in liquid nitrogen.

Crystallography. Diffraction data of PKA-**2** and PKA-**3** were collected at the storage ring Bessy II Helmholtz-Zentrum Berlin, Germany at Beamline 14.1 on a Pilatus 6 M pixel detector. Data of PKA-**1** were collected at the European Synchrotron Radiation Facility (ESRF) Grenoble, France at Beamline BM14. The structure of PKA-**5** has been presented previously by us.[18]

Processing, molecular replacement, and refinement were performed as previously described.[18]

Programs used are XDS,[24] CCP4 Phaser[25] with PDB-structure of PKA from *Bos taurus* 1Q8W, Phenix,[26] Coot,[27] PROCHECK,[28] Moleman,[29] and grade Web server.[30,31] Crystallographic tables as well as mFo-DFc-densities of the different ligands are listed in the Supporting Information. Figures were prepared using Pymol.

Isothermal Titration Calorimetry. This method for ITC measurements was previously described.[18] All measurements were repeated three to five times. Buffer dependency was tested for all ligands, and no significant buffer dependence could be detected. ITC data were analyzed using NITPIC and Sedphat.[32,33] Raw data and exact values and standard deviations for ΔG, ΔH, and $-T\Delta S$ are reported in the Supporting Information.

Compound purity was analyzed as described[18] using quantitative nuclear magnetic resonance spectroscopy (qNMR), and in the case of deviation, ligand concentration was corrected accordingly.[34]

Ligands. Ligand **5** was purchased from Uorsy and ligand **1** from Toronto Research Chemicals (TRC). Ligands **2**, **3**, and **4** were synthesized similarly as previously described.[18]

Molecular Dynamics Simulations. MD simulations were performed using the Amber16 suite of programs.[35] All ligands were considered protonated at the amine nitrogen in the bound as well as unbound state, as supported by our previous study.[18,36] Five input conformations were generated for each ligand with Openeye's Omega software[37] version 2.5, invoking the *enumNitrogen* and *enumRing* options. For these, multiconformational RESP charges were calculated using the R.E.D. server.[38] Force-field parameters were assigned based on the GAFF force field.[39] Simulation runs were set up with the *tleap* module as follows. The ligands were placed in truncated octahedral boxes of TIP3P water[40] with a minimal distance between the solute and the box edges of 15 Å distance. The systems were charge-neutralized by adding a chloride ion. The simulation runs were thermalized according to ref 41 except that a Langevin thermostat with a collision frequency of 2 ps^{-1} was used. Snapshots were saved every 2 ps. Productive simulations were performed with the GPU-accelerated version of PMEMD.[42] For each ligand, four independent simulations were run over 4 μs each, except for **5**, which was simulated for 2 μs. The expanded simulation time of **1**−**4** was applied to take into account the impeded conformational sampling due to methylation (see Results). For **3**−**5**, the crystallized conformations were used as starting points for the simulations. For **1**, two alternative conformations were used as starting points, twice each for the four simulations. For **2**, two simulations were started from the crystallized

DOI: 10.1021/acschembio.9b00476
ACS Chem. Biol. 2019, 14, 2585−2594

conformation. The other two simulations were initiated from a conformation that was manually generated from the crystal conformer by a θ_2 rotating of approximately 180° (yielding dihedral state III, see Results), in order to explore conformation space more efficiently.

Analysis of Ligand Conformational Dynamics. The dihedral angles θ_1 and θ_2 and the twisting angle ζ were calculated using the *cpptraj* module of Amber16.[43] ζ is defined as the dihedral (R_1, C_4, C_5, S) with all atoms being part of the isoquinoline moiety (Figure S6). Cremer and Pople puckering parameters[44] were calculated from the trajectories using the *pytraj* interface to *cpptraj*. The algorithm for the calculation was adapted from ref 45. The discrete puckering assigned to each conformer was inferred from the values of the puckering parameters as defined as discrete puckering states in ref 46 (see Supporting Information for details). The accordingly considered ring conformer forms were chair (C), twist-chair (TC), boat (B), and twist-boat (TB). For each form, 14 different puckering states are possible.

Relative conformational free energies were calculated according to eq 1,[47,48] where R is the gas constant, T = 300 K, p_i is the occurrence probability of a given conformation in microstate i, and p_{ref} is the respective largest probability.

$$\Delta G = -RT \ln(p_i/p_{ref}) \quad (1)$$

The microstates were defined as follows. The conformational free energy of puckering, ΔG_{pucker}, was calculated over the 56 possible puckering states (14 states for each of the four forms). The dihedral free energy, ΔG_{dih}, was calculated by binning θ_1 and θ_2 into bins of 4° width (90 bins along each axis), resulting in a total of 8100 states. For the twisting free energy, ΔG_{twist}, the twisting angle ζ was binned using the same binning parameters as for the dihedral angles.

Conformational entropies were calculated according to eq 2,[47] where the sum runs over the n discrete microstates as defined above.

$$TS_{conf} = -RT \sum_{i=1}^{n} p_i \ln p_i \quad (2)$$

S_{conf} depends on the partitioning of the configuration space.[47] The bin width of 4° used here is within the recommended range of 1° to 5°.[48] Furthermore, an assessment of the bin width influence demonstrated that, while the absolute conformational entropy increases with an increasing number of bins, as expected (Figure S5, left panel), the relative conformational entropies remain nearly constant for different ligands for bin sizes between 1° and 10° (Figure S5, right panel); these bin sizes are similar to values recommended in the literature.[48] Importantly, entropy is defined in terms of the probability density functions over atomic positions in Cartesian space, and conversion to other coordinate systems usually requires a Jacobian.[47,49,50] For configurational entropies calculated from torsions, this Jacobian depends only upon bond lengths and angles, which are rather rigid and can therefore be omitted.[49,51] This assumption is not valid for the puckering entropies such that these values were calculated by Jacobian scaling as described in the Supporting Information. Nevertheless, it must be noted that the resulting entropies TS_{pucker}, TS_{twist}, and TS_{dih} are calculated for different microstates and are thus quantitatively not comparable between each other, such that only differences between ligands are meaningful. Finally, note that the calculation of (absolute) free energies and entropies from MD simulations is a generally difficult problem.[52] This is particularly true for entropic contributions calculated via eq 2, because here ln p_i has to be computed, for which the value of p_i depends not only on microstate i but also on the entire ensemble via the partition function, and conventional MD simulations may not adequately sample high-energy microstates. The problem is alleviated if relative free energies and entropies are considered for similar systems and long MD simulations are used that cover the relevant microstates.[52] Still, considering all this, we only make qualitative comparisons between conformational free energies and entropies between ligands.

■ ASSOCIATED CONTENT

Supporting Information

The Supporting Information is available free of charge on the ACS Publications website at DOI: 10.1021/acschembio.9b00476.

Crystallography: difference density of bound ligands, crystallographic table of data collection and refinement, ITC data, and thermograms; conformational analysis based on MD simulations: ring puckering, evaluation of torsional angle distributions, calculation of puckering entropies, assignment of puckering states, assignment of discrete dihedral states from dihedral angles θ_1 and θ_2; supplementary results: dependence of the conformational entropy on the microstate definition in the θ_1−θ_2 space and geometry of the nitrogen of the sulfonamide group (PDF)

Accession Codes

Atomic coordinates and experimental details for the crystal structures of **1**−**5**, 5M6V, 5M6Y, 5M75, 5M71, and 5LCP will be released upon publication.

■ AUTHOR INFORMATION

Corresponding Author

*Phone: +49 6421 28 21313. E-mail: klebe@staff.uni-marburg.de.

ORCID

Barbara Wienen-Schmidt: 0000-0001-9994-6717
Denis Schmidt: 0000-0001-7319-3462
Andreas Heine: 0000-0002-5285-4089
Holger Gohlke: 0000-0001-8613-1447
Gerhard Klebe: 0000-0002-4913-390X

Notes

The authors declare no competing financial interest.

■ ACKNOWLEDGMENTS

We acknowledge funding from the European Research Council (ERC) of the European Union, Project Number 268145 (DrugProfilBind) and the LOEWE Research Cluster SynChemBio of the Federal State of Hesse (Germany). Furthermore, we acknowledge support from and synchrotron beamtime at BESSY II Helmholtz-Zentrum Berlin in Berlin, Germany and from European Synchrotron Radiation Facility (ESRF), Grenoble. Computational resources and technical support were provided by HRZ Marburg. Furthermore, we gratefully acknowledge the computational support provided by the "Center for Information and Media Technology" (ZIM) at the Heinrich Heine University Düsseldorf, financial support by DFG for funds (grant INST 208/704-1 FUGG to H.G.) to purchase the hybrid computer cluster used in this study, and the computing time provided by the John von Neumann Institute for Computing (NIC) on the supercomputer JURECA at Jülich Supercomputing Centre (JSC; user ID: HKF7). We are grateful to OpenEye for an academic license.

■ ABBREVIATIONS

Ala, alanine; Asp, aspartate; Arg, arginine; ATP, adenosine triphosphate; CHO, Chinese hamster ovary; DFG, aspartate-phenylalanine-glycine motif; DMSO, dimethyl sulfoxide; DTT, dithiothreitol; EDTA, ethylenediaminetetraacetic acid; Gly, glycine; Gly-loop, glycine-rich loop; Glu, glutamate; His-tag, histidine-tag; ITC, isothermal titration calorimetry; MBT,

DOI: 10.1021/acschembio.9b00476
ACS Chem. Biol. 2019, 14, 2585−2594

MES/Bis-Tris; MPD, 2-methyl-2,4-pentanediol; Ni-NTA, nickel-nitrilotriacetic acid; PDB, protein data bank; PKA, cAMP-dependent protein kinase; PKI, protein kinase inhibitor; qNMR, quantitative nuclear magnetic resonance spectroscopy; Ser, serine; TEA, triethanolamine; TEV, tobacco etch virus; Thr, threonine; Val, valine

REFERENCES

(1) Freire, E. (2008) Do enthalpy and entropy distinguish first in class from best in class? *Drug Discovery Today 13*, 869−874.

(2) Ladbury, J. E., Klebe, G., and Freire, E. (2010) Adding calorimetric data to decision making in lead discovery: a hot tip. *Nat. Rev. Drug Discovery 9*, 23−27.

(3) Kawasaki, Y., and Freire, E. (2011) Finding a better path to drug selectivity. *Drug Discovery Today 16*, 985−990.

(4) Núñez, S., Venhorst, J., and Kruse, C. G. (2012) Target-drug interactions: first principles and their application to drug discovery. *Drug Discovery Today 17*, 10−22.

(5) Klebe, G. (2015) Applying thermodynamic profiling in lead finding and optimization. *Nat. Rev. Drug Discovery 14*, 95−110.

(6) Tarcsay, and Keserü, G. M. (2015) Is there a link between selectivity and binding thermodynamics profiles? *Drug Discovery Today 20*, 86−94.

(7) Leung, C. S., Leung, S. S. F., Tirado-Rives, J., and Jorgensen, W. L. (2012) Methyl effects on protein-ligand binding. *J. Med. Chem. 55*, 4489−4500.

(8) Barreiro, E. J., Kümmerle, A. E., and Fraga, C. A. M. (2011) The methylation effect in medicinal chemistry. *Chem. Rev. 111*, 5215−5246.

(9) Schönherr, H., and Cernak, T. (2013) Profound Methyl Effects in Drug Discovery and a Call for New C−H Methylation Reactions. *Angew. Chem., Int. Ed. 52*, 12256−12267.

(10) Bain, J., Plater, L., Elliott, M., Shpiro, N., Hastie, C. J., Mclauchlan, H., Klevernic, I., Arthur, J. S. C., Alessi, D. R., and Cohen, P. (2007) The selectivity of protein kinase inhibitors: a further update. *Biochem. J. 408*, 297−315.

(11) Luo, T., Masson, K., Jaffe, J. D., Silkworth, W., Ross, N. T., Scherer, C. A., Scholl, C., Fröhling, S., Carr, S. A., Stern, A. M., Schreiber, S. L., and Golub, T. R. (2012) STK33 kinase inhibitor BRD-8899 has no effect on KRAS-dependent cancer cell viability. *Proc. Natl. Acad. Sci. U. S. A. 109*, 2860−2865.

(12) Ikenoya, M., Hidaka, H., Hosoya, T., Suzuki, M., Yamamoto, N., and Sasaki, Y. (2002) Inhibition of Rho-kinase-induced myristoylated alanine-rich C kinase substrate (MARCKS) phosphorylation in human neuronal cells by H-1152, a novel and specific Rho-kinase inhibitor. *J. Neurochem. 81*, 9−16.

(13) Nishio, M., Watanabe, Y., and Hidaka, H. (1998) HMN-1180, a small molecule inhibitor of neuronal nitric oxide synthase. *J. Pharmacol. Exp. Ther. 287*, 1063−1067.

(14) Jacobs, M., Hayakawa, K., Swenson, L., Bellon, S., Fleming, M., Taslimi, P., and Doran, J. (2006) The structure of dimeric ROCK I reveals the mechanism for ligand selectivity. *J. Biol. Chem. 281*, 260−268.

(15) Tamura, M., Nakao, H., Yoshizaki, H., Shiratsuchi, M., Shigyo, H., Yamada, H., Ozawa, T., Totsuka, J., and Hidaka, H. (2005) Development of specific Rho-kinase inhibitors and their clinical application. *Biochim. Biophys. Acta, Proteins Proteomics 1754*, 245−252.

(16) Yamaguchi, H., Kasa, M., Amano, M., Kaibuchi, K., and Hakoshima, T. (2006) Molecular mechanism for the regulation of rho-kinase by dimerization and its inhibition by fasudil. *Structure 14*, 589−600.

(17) Shibuya, M., Asano, T., and Sasaki, Y. (2001) Effect of FasudilHCl, a Protein Kinase Inhibitor, on Cerebral Vasospasm, in *Cerebral Vasospasm*, pp 201−204, Springer, Vienna.

(18) Wienen-Schmidt, B., Jonker, H. R., Wulsdorf, T., Gerber, H.-D., Saxena, K., Kudlinzki, D., Sreeramulu, S., Parigi, G., Luchinat, C., Heine, A., Schwalbe, H., and Klebe, G. (2018) Paradoxically, Most Flexible Ligand Binds Most Entropy-Favored: Intriguing Impact of Ligand Flexibility and Solvation on Drug−Kinase Binding. *J. Med. Chem. 61*, 5922−5933.

(19) Breitenlechner, C., Gassel, M., Hidaka, H., Kinzel, V., Huber, R., Engh, R. A., and Bossemeyer, D. (2003) Protein kinase A in complex with Rho-kinase inhibitors Y-27632, Fasudil, and H-1152P: structural basis of selectivity. *Structure 11*, 1595−1607.

(20) Bonn, S., Herrero, S., Breitenlechner, C. B., Erlbruch, A., Lehmann, W., Engh, R. A., Gassel, M., and Bossemeyer, D. (2006) Structural analysis of protein kinase A mutants with Rho-kinase inhibitor specificity. *J. Biol. Chem. 281*, 24818−24830.

(21) Gilsbach, B. K., Ho, F. Y., Vetter, I. R., van Haastert, P. J. M., Wittinghofer, A., and Kortholt, A. (2012) Roco kinase structures give insights into the mechanism of Parkinson disease-related leucine-rich-repeat kinase 2 mutations. *Proc. Natl. Acad. Sci. U. S. A. 109*, 10322−10327.

(22) Kawasaki, Y., Chufan, E. E., Lafont, V., Hidaka, K., Kiso, Y., Mario Amzel, L., and Freire, E. (2010) How much binding affinity can be gained by filling a cavity? *Chem. Biol. Drug Des. 75*, 143−151.

(23) Kudlinzki, D., Linhard, V. L., Saxena, K., Sreeramulu, S., Gande, S., Schieborr, U., Dreyer, M., and Schwalbe, H. (2015) High-resolution crystal structure of cAMP-dependent protein kinase from Cricetulusgriseus. *Acta Crystallogr., Sect. F: Struct. Biol. Commun. 71*, 1088−1093.

(24) Kabsch, W. (2010) XDS. *Acta Crystallogr., Sect. D: Biol. Crystallogr. 66*, 125−132.

(25) McCoy, A. J., Grosse-Kunstleve, R. W., Adams, P. D., Winn, M. D., Storoni, L. C., and Read, R. J. (2007) Phaser crystallographic software. *J. Appl. Crystallogr. 40*, 658−674.

(26) Adams, P. D., Afonine, P. V., Bunkóczi, G., Chen, V. B., Davis, I. W., Echols, N., Headd, J. J., Hung, L.-W., Kapral, G. J., Grosse-Kunstleve, R. W., McCoy, A. J., Moriarty, N. W., Oeffner, R., Read, R. J., Richardson, D. C., Richardson, J. S., Terwilliger, T. C., and Zwart, P. H. (2010) PHENIX: a comprehensive Python-based system for macromolecular structure solution. *Acta Crystallogr., Sect. D: Biol. Crystallogr. 66*, 213−221.

(27) Emsley, P., Lohkamp, B., Scott, W. G., and Cowtan, K. (2010) Features and development of Coot. *Acta Crystallogr., Sect. D: Biol. Crystallogr. 66*, 486−501.

(28) Laskowski, R. A., MacArthur, M. W., Moss, D. S., and Thornton, J. M. (1993) PROCHECK: a program to check the stereochemical quality of protein structures. *J. Appl. Crystallogr. 26*, 283−291.

(29) Kleywegt, G. J., Zou, J.-Y., Kjeldgaard, M., and Jones, T. A. (2001) Around O, in *International Tables for Crystallography Vol. F: Crystallography of biological macromolecules*, pp 353−356, Springer, The Netherlands.

(30) Smart, O. S., Womack, T. O., Sharff, A., Flensburg, C., Keller, P., Paciorek, W., Vonrhein, C., and Bricogne, G. Global Phasing Limited. http://www.globalphasing.com.

(31) Bruno, I. J., Cole, J. C., Kessler, M., Luo, J., Motherwell, W. D. S., Purkis, L. H., Smith, B. R., Taylor, R., Cooper, R. I., Harris, S. E., and Orpen, A. G. (2004) Retrieval of crystallographically-derived molecular geometry information. *J. Chem. Inf. Model. 44*, 2133−2144.

(32) Keller, S., Vargas, C., Zhao, H., Piszczek, G., Brautigam, C. A., and Schuck, P. (2012) High-precision isothermal titration calorimetry with automated peak-shape analysis. *Anal. Chem. 84*, 5066−5073.

(33) Houtman, J. C. D., Brown, P. H., Bowden, B., Yamaguchi, H., Appella, E., Samelson, L. E., and Schuck, P. (2007) Studying multisite binary and ternary protein interactions by global analysis of isothermal titration calorimetry data in SEDPHAT: application to adaptor protein complexes in cell signaling. *Protein Sci. 16*, 30−42.

(34) Holzgrabe, U., Deubner, R., Schollmayer, C., and Waibel, B. (2005) Quantitative NMR spectroscopy−applications in drug analysis. *J. Pharm. Biomed. Anal. 38*, 806−812.

(35) Case, D. A., Cheatham, T. E., Darden, T., Gohlke, H., Luo, R., Merz, K. M., Onufriev, A., Simmerling, C., Wang, B., and Woods, R. J. (2005) The Amber biomolecular simulation programs. *J. Comput. Chem. 26*, 1668−1688.

DOI: 10.1021/acschembio.9b00476
ACS Chem. Biol. 2019, 14, 2585−2594

(36) Wienen-Schmidt, B., Wulsdorf, T., Jonker, H. R. A., Saxena, K., Kudlinzki, D., Linhard, V., Sreeramulu, S., Heine, A., Schwalbe, H., and Klebe, G. (2018) On the Implication of Water on Fragment-to-Ligand Growth in Kinase Binding Thermodynamics. *ChemMedChem 13*, 1988−1996.
(37) Hawkins, P. C. D., Skillman, A. G., Warren, G. L., Ellingson, B. A., and Stahl, M. T. (2010) Conformer Generation with OMEGA: Algorithm and Validation Using High Quality Structures from the Protein Databank and Cambridge Structural Database. *J. Chem. Inf. Model. 50*, 572−584.
(38) Vanquelef, E., Simon, S., Marquant, G., Garcia, E., Klimerak, G., Delepine, J. C., Cieplak, P., and Dupradeau, F.-Y. (2011) R.E.D. Server: a web service for deriving RESP and ESP charges and building force field libraries for new molecules and molecular fragments. *Nucleic Acids Res. 39*, W511−W517.
(39) Wang, J., Wolf, R. M., Caldwell, J. W., Kollman, P. A., and Case, D. A. (2004) Development and testing of a general amber force field. *J. Comput. Chem. 25*, 1157−1174.
(40) Jorgensen, W. L. (1982) Revised TIPS for simulations of liquid water and aqueous solutions. *J. Chem. Phys. 77*, 4156−4163.
(41) Schmidt, D., Boehm, M., McClendon, C. L., Torella, R., and Gohlke, H. (2019) Cosolvent-enhanced Sampling and Unbiased Identification of Cryptic Pockets Suitable for Structure-based Drug Design. *J. Chem. Theory Comput. 15*, 3331−3343.
(42) Salomon-Ferrer, R., Götz, A. W., Poole, D., Le Grand, S., and Walker, R. C. (2013) Routine Microsecond Molecular Dynamics Simulations with AMBER on GPUs. 2. Explicit Solvent Particle Mesh Ewald. *J. Chem. Theory Comput. 9*, 3878−3888.
(43) Roe, D. R., and Cheatham, T. E. (2013) PTRAJ and CPPTRAJ: Software for Processing and Analysis of Molecular Dynamics Trajectory Data. *J. Chem. Theory Comput. 9*, 3084−3095.
(44) Cremer, D., and Pople, J. A. (1975) A General Definition of Ring Puckering Coordinates. *J. Am. Chem. Soc. 97*, 1354−1358.
(45) Hill, A. D., and Reilly, P. J. (2007) Puckering Coordinates of Monocyclic Rings by Triangular Decomposition. *J. Chem. Inf. Model. 47*, 1031−1035.
(46) Boessenkool, I. K., and Boeyens, J. C. A. (1980) Identification of the conformational type of seven-membered rings. *J. Cryst. Mol. Struct. 10*, 11−18.
(47) Zhou, H.-x., and Gilson, M. K. (2009) Theory of Free Energy and Entropy in Noncovalent Binding. *Chem. Rev. 109*, 4092−4107.
(48) Polyansky, A. A., Zubac, R., and Zagrovic, B. (2012) *Estimation of Conformational Entropy in Protein-Ligand Interactions: A Computational Perspective*, pp 327−353, Springer, New York.
(49) Baxa, M. C., Haddadian, E. J., Jumper, J. M., Freed, K. F., and Sosnick, T. R. (2014) Loss of conformational entropy in protein folding calculated using realistic ensembles and its implications for NMR-based calculations. *Proc. Natl. Acad. Sci. U. S. A. 111*, 15396−15401.
(50) Hnizdo, V., and Gilson, M. K. (2010) Thermodynamic and Differential Entropy under a Change of Variables. *Entropy 12*, 578−590.
(51) Killian, B. J., Yundenfreund Kravitz, J., and Gilson, M. K. (2007) Extraction of configurational entropy from molecular simulations via an expansion approximation. *J. Chem. Phys. 127*, 024107−024107.
(52) Meirovitch, H. (2007) Recent developments in methodologies for calculating the entropy and free energy of biological systems by computer simulation. *Curr. Opin. Struct. Biol. 17*, 181−186.

DOI: 10.1021/acschembio.9b00476
ACS Chem. Biol. 2019, 14, 2585−2594